Journal of Fluids and Structures 17 (2003) 941–953

JOURNAL OF
FLUIDS AND
STRUCTURES

www.elsevier.nl/locate/jnlabr/yjfls

Temporal flow instability for Magnus–Robins effect at high rotation rates ☆

T.K. Sengupta[a,]*, A. Kasliwal[a], S. De[a], M. Nair[b]

[a] *CFD Laboratory, Department of Aerospace Engineering, Indian Institute of Technology Kanpur, Kanpur 208 016, India*
[b] *National Aerospace Laboratories, Bangalore, India*

Received 2 April 2002; accepted 14 March 2003

Abstract

The lift and drag coefficients of a circular cylinder, translating and spinning at a supercritical rate is studied theoretically to explain the experimentally observed violation of maximum mean lift coefficient principle, that was proposed heuristically by Prandtl on the basis of inviscid flow model. It is also noted experimentally that flow past a rotating and translating cylinder experiences temporal instability—a fact not corroborated by any theoretical studies so far. In the present paper we report very accurate solution of Navier–Stokes equation that displays the above-mentioned instability and the violation of the maximum limit. The calculated lift coefficient exceeds the limit of 4π, instantaneously as well as in time-averaged sense. The main purpose of the present paper is to explain the observed temporal instability sequence in terms of a new theory of instability based on full Navier–Stokes equation that does not require making any assumption about the flow field, unlike other stability theories.

1. Introduction

The two-dimensional flow field generated by an infinitely long circular cylinder of diameter D translating with an uniform velocity U_∞ at right angles to its axis and rotating about this axis with angular velocity Ω^* has been studied by various researchers for a long time. The two important parameters of these studies are the Reynolds number given by, $\mathrm{Re} = U_\infty D/\nu$ with ν as the coefficient of kinematic viscosity and the ratio of the peripheral to translational speed, $\Omega = \Omega^* D/(2U_\infty)$ of the circular cylinder.

The fact that a projectile spinning about its axis of travel experiences a transverse force (lift) was originally reported by Robins (1761) and later by Magnus (1853). The former work is not well known although an interesting account of this is provided in Anderson (1997). The complex flow field generated by this seemingly simple geometry has served as a test case to understand the lift generation mechanism and unsteady separation in innumerable studies including in Reid (1924), Prandtl (1926), Thom (1931), Tokumaru and Dimotakis (1993) and Diaz et al. (1983).

For potential flow, the lift experienced by an airfoil is modelled by fixing the rear stagnation point at the trailing edge where the physical body has a sharp change in curvature. For bodies with rounded trailing edges, this model cannot be used. However, Prandtl (1926) argued that for a rotating cylinder the maximum circulation that can be created corresponds to a situation when the rear and front stagnation points join at the bottom of the cylinder constituting a half-saddle point. For potential flow this produces a $C_{L_{\max}} = 4\pi$ corresponding to $\Omega = 2$ (critical rotation rate). In this model of potential flow any further increase of Ω will not cause further increase of C_L. This is due to the fact that the

---

☆ An earlier version of this paper was submitted to this journal on 31 August 1998.

*Corresponding author.

E-mail address: tksen@iitk.ac.in (T.K. Sengupta).

0889-9746/03/$ - see front matter © 2003 Elsevier Ltd. All rights reserved.
doi:10.1016/S0889-9746(03)00052-5

half-saddle point transforms into a full saddle point inside the flow domain when Ω is increased further and the flow inside the closed recirculating zone cannot shed any circulation outside the streamline containing the full saddle point.

This heuristic argument put forth by Prandtl (1926), by using an inviscid flow model, for the maximum lift of a real flow has been found wanting by Tokumaru and Dimotakis (1993), who reported experimentally measured maximum lift exceeding by 20% for $\Omega = 10$ and $\mathrm{Re} = 3800$. The authors considered diffusion, unsteady flow processes and three-dimensional end-effects as likely causes for this supposed violation. In a similar experiment, Werle (1984) has also reported observing, at high supercritical rotation rate for $\mathrm{Re} = 3300$, a layer of rotating fluid next to the surface of the cylinder which subsequently suffered more or less periodic instabilities.

The above experimental observations indicate that unsteady full Navier–Stokes equation needs to be solved. Some of the recent works in this area, among many others, are due to Badr et al. (1990), Chew et al. (1995) and Nair et al. (1998). Furthermore, it is also necessary that the numerical procedure for such simulations must be accurate to capture the experimentally observed instabilities reported in Werle (1984). Some preliminary computations showing the presence of instabilities have been reported in Sengupta et al. (1999) for a range of Reynolds numbers and rotational rates. The primary aim of this research is to explain the origin of this instability.

Quite a number of other experimental efforts have been reported in the literature on flow past rotating circular cylinders, some of which have already been discussed. Apart from McLaughlin et al. (1991), Chew (1987) has measured the pressure distributions around a rotating cylinder directly by using a single pressure transducer.

Note that the results presented in Chew et al. (1995) for the lift do not match qualitatively with the results reported in Tokumaru and Dimotakis (1993) for high rotation rates. While the reason was attributed to three dimensionality of the flow, some remarks are in order about the hybrid vortex method used by them. The hybrid vortex method is a combination of the diffusion vortex method and the vortex-in-cell method. While the former deals with the full viscous equation in stream-function-vorticity formulation close to the body, the later is an inviscid method due to Christiansen (1973), applied in the exterior part of the domain. In the diffusion vortex method the governing equations are advanced in time by splitting the process of convection and diffusion independently. Additionally, the vortices that are generated, diffused and convected are redistributed to the fixed mesh points. According to Chew et al. (1995) this process itself can give rise to large numerical diffusion. It is well known that the redistribution is necessary to control the integration errors associated with ever-increasing population of discrete vortices which otherwise lead to a chaotic solution (see Sarpkaya 1989, 1994). As has been described very lucidly by Sarpkaya (1989), this type of techniques "can slow down the effects of the discrete form of the Helmholtz instability…but do not make the vortex-sheet methods convergent. Furthermore, they introduce some diffusion of vorticity, either along or away from the sheet and hence errors into the calculations at all wavelengths". Similarly the vortex-in-cell method also can contribute to pseudo-viscosity, according to Chew et al. (1995).

Another cause for disagreement with experimental results may also be due to the way the surface pressure is usually calculated for two-dimensional flows. A very clear account for this is given in Pan and Chew (2002), where the authors identify the problem with the numerical procedure of differentiation of vorticity, when the surface pressure is calculated from the vorticity derivative by a simple quadrature. Two other methods for calculating the surface pressure are also discussed in Pan and Chew (2002). One requires estimation of surface pressure from the pressure–velocity formulation of Navier–Stokes equation and the other from the solution of pressure Poisson equation. Roache (1976) has also noted that the evaluation of pressure by the first method gives "different answers when different paths are used to get to the same point. The discrepancy will be partly due to solution errors for ψ. But even if the exact solution values for ψ were known at all mesh points, different paths of integration would yield different answers due to quadrature errors. Further, note that velocity gradients are integrated…requiring double differentiation of the numerically obtained stream function, which is usually inaccurate…. A more accurate solution can be determined from the Poisson form of the pressure equation". In the present work we have solved the governing Poisson equation for pressure. Since this Poisson equation has to be solved along with a Neumann boundary condition, the solution times are large compared to the stream-function equation that is solved along with a Dirichlet boundary condition. This procedure of solving the pressure Poisson equation was followed in Nair et al. (1998) and Sengupta et al. (1999).

In the next section, a brief description of the governing equations that are solved and the auxiliary conditions are described, along with the numerical method. In Section 3, results and their detailed explanation are provided.

2. Governing equation and boundary conditions

The details of the governing equations and auxiliary conditions are described in Nair et al. (1998) and Nair and Sengupta (1997). They are not repeated here, and only a brief description follows.

Two-dimensional Navier–Stokes equations are solved here in a stream-function and vorticity formulation. The nondimensional form of these equations are given by

$$\nabla^2\psi = -\omega \tag{1}$$

and

$$\frac{\partial\omega}{\partial t} + \nabla\cdot(\omega\mathbf{V}) = \frac{1}{\mathrm{Re}}\nabla^2\omega, \tag{2}$$

where ω is the out-of-plane component of vorticity defined by $\omega = (\nabla\times\mathbf{V})\cdot\hat{k}$ and the velocity is related to the stream function by $\mathbf{V} = \nabla\times\boldsymbol{\psi}$, where $\boldsymbol{\psi} = (0, 0, \psi)$. The flow is computed in the transformed (ξ, η)-plane, where

$$x = r(\eta)\cos 2\pi\xi \quad \text{and} \quad y = r(\eta)\sin 2\pi\xi, \tag{3}$$

in which $0 \leqslant \xi, \eta \leqslant 1$, and

$$r(\eta) = r_0 + \frac{\eta}{\Delta\eta}\left[\Delta r_0 + \frac{d}{2}\left(\frac{\eta}{\Delta\eta} - 1\right)\right], \tag{4}$$

where r_0 indicates the radius of the cylinder, Δr_0 is the spacing of the first radial line and d is the increment of the successive grid line spacing. This type of grid removes alteration of convection and lowest order numerical dissipation, as discussed in Nair et al. (1998).

The governing Poisson equation for total pressure (p_t) is obtained by taking the divergence of the Navier–Stokes equation in primitive variables. For an orthogonal curvilinear coordinate system this is given as

$$\frac{\partial}{\partial\xi}\left(\frac{h_2}{h_1}\frac{\partial p_t}{\partial\xi}\right) + \frac{\partial}{\partial\eta}\left(\frac{h_1}{h_2}\frac{\partial p_t}{\partial\eta}\right) = \frac{\partial}{\partial\xi}(h_2 v\omega) - \frac{\partial}{\partial\eta}(h_1 u\omega), \tag{5}$$

where h_1 and h_2 are the scale factors given by $h_1 = (x_\xi^2 + y_\xi^2)^{1/2}$ and $h_2 = (x_\eta^2 + y_\eta^2)^{1/2}$.

For the boundary conditions on the cylinder wall, the no-slip condition is given by

$$\left(\frac{\partial\psi}{\partial\eta}\right)_{\text{body}} = h_2 r_0 \Omega \tag{6}$$

and

$$\psi = \text{constant}, \tag{7}$$

The conditions given by Eqs. (6) and (7) are used in calculating the wall vorticity, condition (7) is used only in solving the stream-function Eq. (1). The additional periodic boundary condition is applied at the cut (see definition Fig. 1),

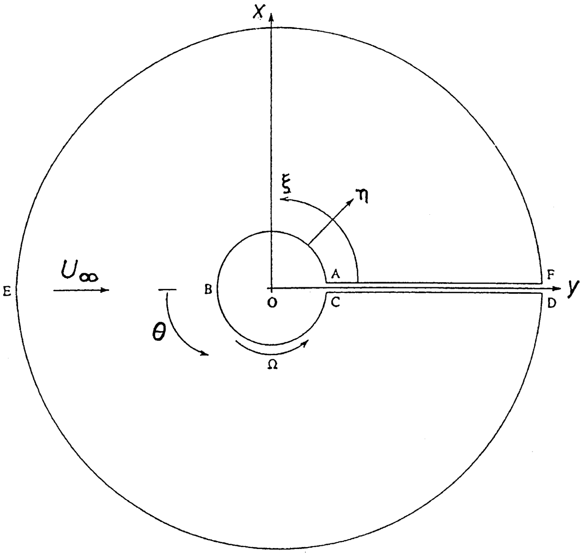

Fig. 1. Schematic of flow around a translating and spinning circular cylinder. Note the reference for measuring θ.

while at the outer boundary, uniform flow conditions are applied. The corresponding far field boundary condition is

$$\frac{\partial \omega}{\partial \eta} = 0. \tag{8}$$

For the pressure Poisson equation, Eq. (5), a Neumann boundary condition, as obtained from the normal (η) momentum equation is used on the surface and outer boundary, whereas a periodic boundary condition is applied at the cut (Fig. 1). The steady-state inviscid solution is taken to be the initial condition for the impulsively started cylinder problem.

In the present work, in order to specifically observe the effects of initial unsteadiness and diffusion, we have computed the cases for Re $= 3800$ at $\Omega = 5$ for two different start-up conditions:

(i) the case of pure impulsively started rotation and translation;
(ii) the alternative case, where the translation to final free stream speed is established by a smooth, but, nonuniform acceleration. The rotation is once again established impulsively. The nonuniform acceleration gives rise to the free-stream speed variation given by a tangent hyperbolic function

$$U_\infty(t) = \bar{U}_\infty \tanh\left(\frac{t}{\tau}\right). \tag{9}$$

For this case the value of τ used is 0.6 (nondimensional convection time scale) and during the initial time up to $t = 0.20$ the acceleration is uniform.

For the pure impulsive start, it is well known that the initial wall vorticity has a square-root singularity. The analytical solution has been given in Badr and Dennis (1985) and Chew et al. (1995) that was obtained by formal perturbation series expansion. An analytical expression for the vorticity at early times can be obtained for the uniform acceleration case, and that shows that there are no such singularities of vorticity. Also, it can be shown that the initial acceleration will have an effect only if it persists beyond the time at which the first separation bubble is formed for any two-dimensional body held stationary in a uniform flow. Thus, the numerical results will be identical if the initial acceleration phase is over before the first bubble forms. This also explains the exact match of the computational results by Badr and Dennis (1985), and Chew et al. (1995). The last reference has the correct expression of initial wall vorticity. In Nair et al. (1998) the wall vorticity is calculated numerically at all times, and this also exhibits an identical numerical solution and a good match with flow visualization results when the flow is truly two dimensional.

For the solution of Poisson Eqs. (1) and (5), the Modified Strongly Implicit Procedure (MSIP) of Schneider and Zedan (1981) and the Conjugate Gradient method are used. In general, the equations are discretized at the cell nodes, while the pressure equation is discretized at the cell centres for the boundary points. The time discretization for Eq. (2) is by an explicit Euler scheme.

3. Results and discussion

The results reported in Tokumaru and Dimotakis (1993) are for Re $= 3800$, while Werle (1984) reported observations for Re $= 3300$. The results reported here are for Re $= 3800$ and 1000, for different rotation rates. A fine grid with 450 points in the radial direction and 271 points in the azimuthal direction is used. The first azimuthal line is 0.0005D away from the cylinder, and the outer boundary is located 24 diameters from the cylinder. A nondimensional time step of 0.0001 was used for numerically advancing the solution. The schematic and notations are shown in Fig. 1. The present grid is finer compared to the (128×120) grid used by Chen et al. (1993), Badr and Dennis (1985) and Badr et al. (1990); all these studies used the stream-function-vorticity formulation. Badr and Dennis (1985) and Badr et al. (1990) took a value of Δz of 0.05 in the initial stages and 0.1 beyond $t = 1.5$, where z is the radial distance nondimensionalized by the viscous length scale (usually defined for unsteady boundary layer flows). Because they used a fixed maximum value of z, the radial spacing became coarser with time as the boundary layer thickened with time.

Although most of the computations reported for the rotating cylinder cases use impulsively started condition, the corresponding laboratory experiments reveal conditions that are not strictly impulsive. For example, for the experimental set-up described in Coutanceau and Menard (1985), it is easy to see that the start-up time (maximum) to establish the final free-stream speed is 1/8th of the convection time scale. In Nair et al. (1998), a detailed discussion on this aspect is given, where it is stated that for computing the cases reported in Coutanceau and Menard (1985), one can take the start-up as impulsive without incurring any error. Here we investigate the role of start-up processes for the Magnus–Robins effect. The streamlines plotted in this paper are in a translating frame of reference, as in experiments. In Fig. 2, streamline contours are shown for Re $= 1000$ and $\Omega = 3.0$ to show a typical result along with the corresponding flow visualization picture from Coutanceau and Menard (1985). The detailed comparison with

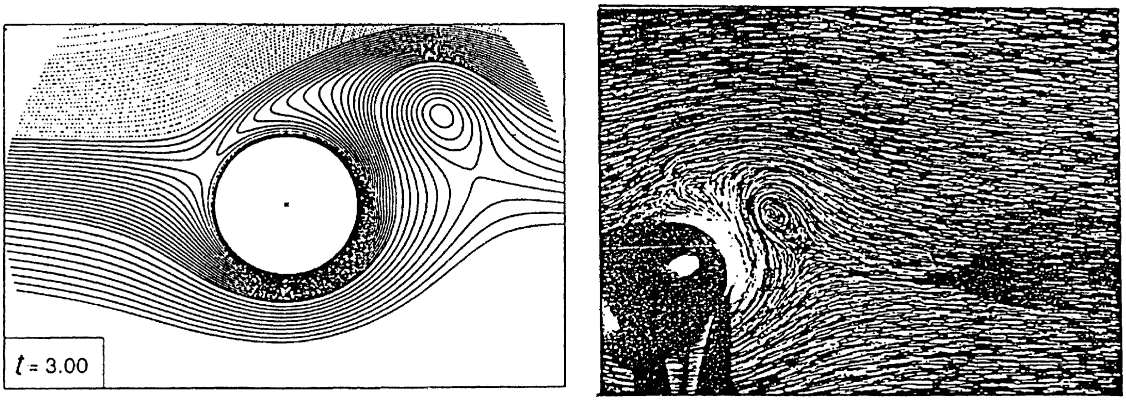

Fig. 2. Computed and experimental instantaneous streamline contours at $t = 3$ for Re = 1000 and $\Omega = 3$. The experimental result is from Coutanceau and Menard (1985).

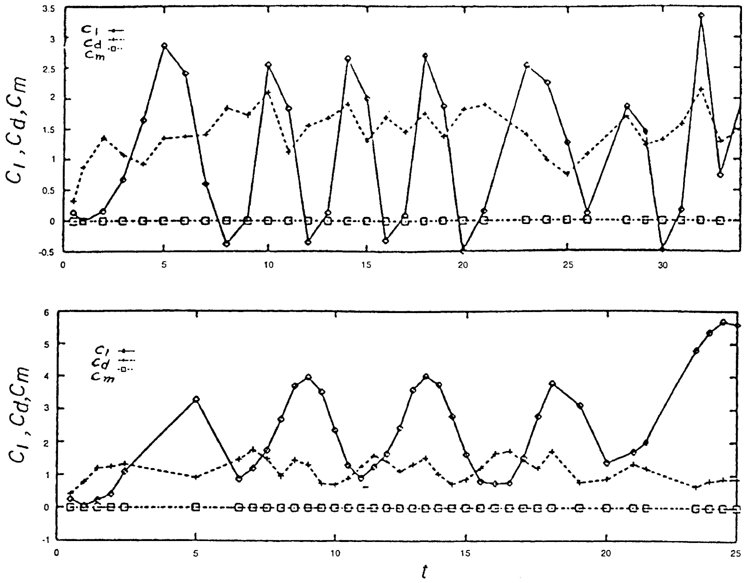

Fig. 3. Lift, drag and pitching moment coefficients for Re = 3800 and $\Omega = 0.5$(top) and 1.0 (bottom), as a functions of time.

experimental results are given in Nair et al. (1998) for other Reynolds numbers and rotation rates. The accuracy and stability of the numerical schemes used has been addressed in Nair and Sengupta (1997) and Sengupta and Nair (1999) in greater detail for the upwind scheme used here.

Here Fig. 2 is shown for a special feature of the experiment of Coutanceau and Menard (1985). There is a general resemblance of the computed field with the experimental visualization. However, there are differences in the shape of the streamlines upstream of the detached vortex. Similar differences have also been reported by other authors (see e.g. Badr et al., 1990), and such differences were more pronounced at later times. Polidori et al. (1993) have published results using the same experimental facility for a stationary cylinder for Re = 1000. Fig. 3 of their paper reveals the creation of vortices at the junction of the model and the tunnel wall. These structures move towards the centre-line with the passage of time, rendering the flow three dimensional. A visualization picture taken from one side of tunnel records streamlines at multiple spanwise stations, giving the appearance of the experimental picture shown in Fig. 2. This is the reason that all two-dimensional calculations show very good agreement of the detached vortex, but none show a good match of flow at the shoulder of the cylinder.

3.1. The cases for Re=3800 and $\Omega = 0.5$ and 1.0

Some preliminary results were given in Nair et al. (1998) for the case of $\Omega = 2$ and $\mathrm{Re} = 3800$. In Fig. 3 the loads for the two cases of $\Omega = 0.5$ and 1.0 are shown for early times only. It should be mentioned that the issues of grid dependence and numerical instabilities associated with the higher-order finite difference method are resolved and reported in Nair et al. (1998). In the same way, it has been ensured that the results presented are grid independent and the time integration proceeded without numerical instability for long times. For lower rotation cases one notices the formation of an *alleyway* on the top-side that pushes the vortices towards the bottom half. Perry et al. (1982) have coined the term *alleyway* in explaining the near-wake behaviour by examining instantaneous streamlines. An *alleyway* refers to meandering of the streamline(s) in the near-wake to the opposite half of the flow after encircling vortices in the wake. The presence of an *alleyway* implies that the flow has turned sharply near the body and that is the reason for the lift direction reversal at irregular intervals.

For the case of $\Omega = 1$ the *alleyways* are formed predominantly on the bottom half. The results for the $\Omega = 2$ case, for which inviscid theory predicts that the front and rear stagnation points will be coincident, was discussed in Nair et al. (1998). The following discussion is based on the results of the same reference. According to inviscid flow theory the lift would not change once the closed streamline is formed. However, this is an unsteady viscous flow, where vorticity is continually generated at the wall, and even after the formation of the closed streamline, the wall vorticity keeps changing and hence circulation also changes continually. Beyond $t = 5$ the closed streamline opens up and at $t = 5.5$ and beyond one can notice a tongue-shaped *alleyway* forming on the windward side of the cylinder. In contrast, the *alleyways* for the lower rotation cases are always on the leeward side. Prandtl (1926) suggested that, as rotation rate increases, the front and rear stagnation points approach each other and, once they merge for $\Omega = 2$, no further increase in lift is possible, since the flow inside and outside are insulated from each other. Such an argument has also been repeated by Tokumaru and Dimotakis (1993), who have furthermore added that such insulation can be violated only if the “outside flow” can receive vorticity from “inside flow” through spanwise migration of information. It is in this way that the lift coefficient can exceed the theoretical maximum lift coefficient value of 4π. However, such an argument cannot explain why and how the closed streamline can increase in size and also change its shape for rotation rates higher than $\Omega = 2$. We will come back to this discussion again, while talking about the results for the higher rotation rate of $\Omega = 5$. However, looking at the instantaneous streamlines and the lift value for $\Omega = 2$ case, one can observe a direct correlation between the size of the recirculating bubble and the lift experienced by the cylinder. Qualitatively, the presence of a closed streamline for viscous flow can be related to an equivalent inviscid flow past a cylinder of increased size. This effective size is determined by the stability of the closed streamline shape and is a direct function of the rotation rate. Higher rotation rates allow formation of a larger equivalent size of the closed streamline during the transient state. These results clearly demonstrate the role of unsteadiness for this flow configuration, with its attendant cycle of closed streamline formation followed by *alleyway* formation, in the windward side.

3.2. The case for Re =3800; $\Omega = 5$

This case of higher rotation rate is studied as it enables one to follow the unsteady load development. For example the experimental results due to Tokumaru and Dimotakis (1993) exhibit an increase of the time-averaged lift as the rotation rate increases. At the same time, Chew et al. (1995) have reported computed results for $\mathrm{Re} = 1000$, where the lift coefficient levels-off with increasing rotation rate (see their Fig. 26).

First of all, the cases of two different start-ups are investigated. The first start-up is the usual impulsive start of the flow and for the second case the free-stream speed increases with a smooth acceleration, as given by Eq. (9). The loads are shown up to a nondimensional time of $t = 30$ in Fig. 4 for these two start-ups. The two different start-ups yield the same load levels and the same sequence of instabilities. What is rather revealing in Fig. 4 is that the lift drops by about 50% after $t = 27.90$ over a very small time, while the drag increases during the corresponding period. The abruptness of these changes can be well appreciated if we note that for a cylinder of 1 cm diameter placed in a free stream of 10 m/s the convection time scale is 1 ms. This is also the scale we have used to nondimensionalize the vorticity transport equation. Hence, the abrupt fall in the lift occurs over a small time interval of less than 2 ms, as indicated in our computations.

In Fig. 5 the variation of c_l and c_d is shown for a long time interval. It is to be noted that the long time average of lift coefficient depicted in Fig. 5 matches with the experimentally measured value of lift by Tokumaru and Dimotakis (1993). Also the displayed lift and drag curves show repeated instabilities referred to in Werle (1984). The loss of lift starts after $t = 27.67$ and continues to fall till $t = 30.0$ and a similar sequence of events occur after $t = 56$ and at $t = 85$. The lift at $t = 29.9$ has fallen by 46.1% from the peak value of lift attained before the fall. The drop of lift, during subsequent instabilities, is smaller as compared to that during the first instability. This is perhaps due to the dynamical

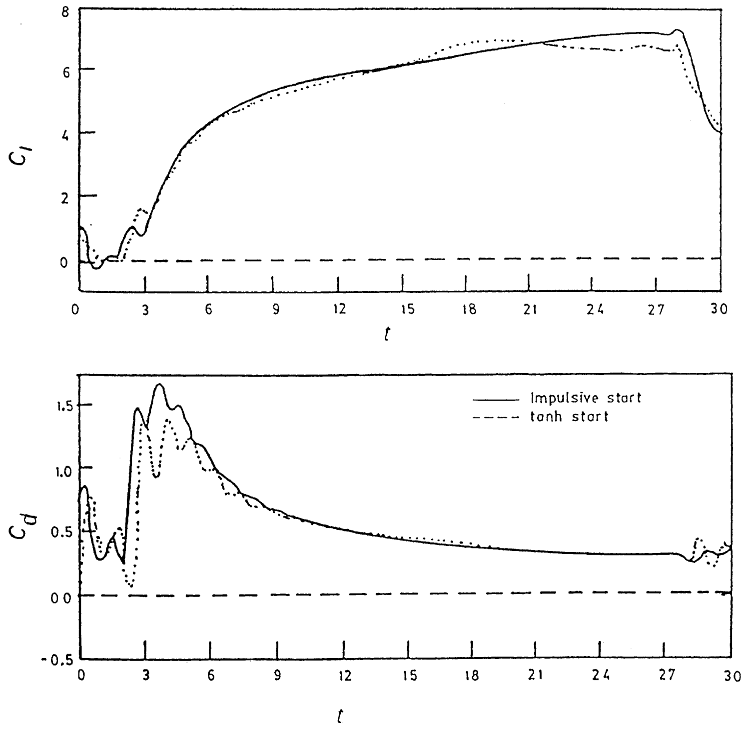

Fig. 4. Lift and drag coefficients for Re = 3800 and $\Omega = 5$ as a function of time for an impulsive and an accelerated start for the oncoming flow, given by Eq. (9).

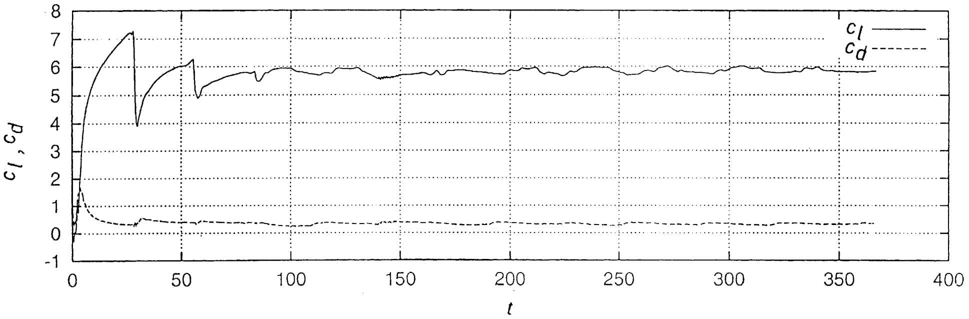

Fig. 5. Long-time variation of lift and drag coefficients for Re = 3800 and $\Omega = 5$ for impulsive start.

system adjusting itself in terms of a stable vorticity distribution in the flow field. Thus, the first instability is studied in the following.

For the impulsive start case, some representative instantaneous streamline and vorticity contours are shown in Fig. 6 at some representative times during and after the first instability. In these figures the flow is from the right to the left. Generally, for subcritical rotation rates, the front and rear stagnation points move towards the bottom while remaining on the cylinder surface, if the rotation rate is increased. These stagnation points are also called the half-saddle points. These half-saddle points are asymmetric with respect to the vertical axis due to the drag experienced by the cylinder. With an increase of rotation rate to the critical value, the half-saddle points merge with each other at the bottom of the cylinder, on its surface. Any further increase in rotation rate causes the merged half-saddle point to move inside the flow domain, forming what is called the full-saddle point. The present case corresponds to a super-critical rotation rate, and hence one can see closed streamlines around the cylinder enclosed by the streamline contour that contains the full saddle point.

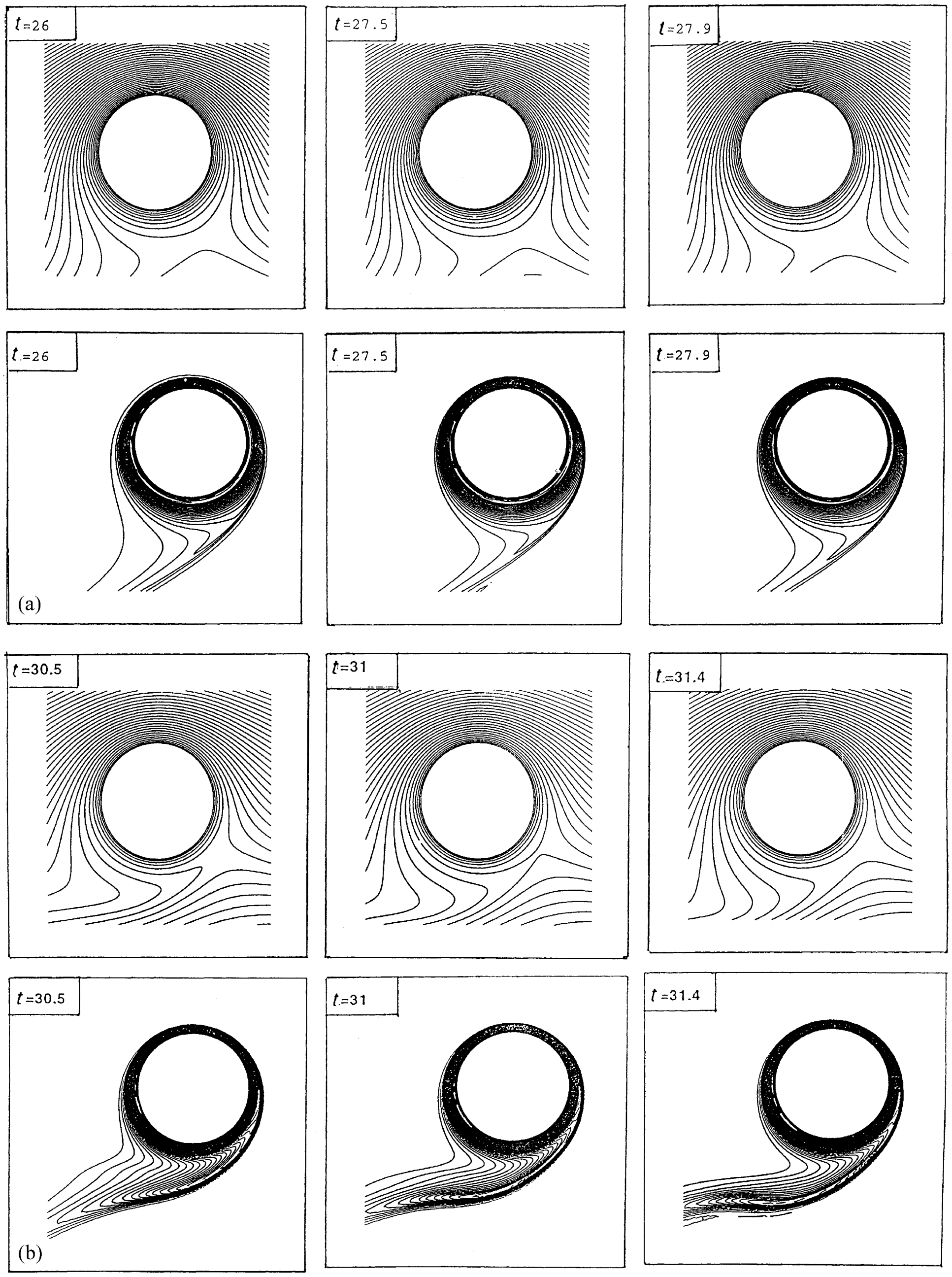

Fig. 6. Instantaneous streamline-contours (top) and vorticity-contours (bottom) at indicated times for the $\mathrm{Re} = 3800$ and $\Omega = 5$ case.

Vorticity is continually generated at the no-slip wall that is convected and diffused, as governed by the Navier–Stokes equation. Initially, the lift increases because the circulation generation is more than its diffusion and convection. Accumulating vorticity in the neighbourhood of the wall becomes unstable, resulting in expulsion of vorticity from the recirculating pool of fluid next to the cylinder surface. In the present context, small disturbances are due to various numerical sources. This instability is manifested by detachment of vortices from the rotating pool of fluid. The signature of this event is in the vorticity contour plots shown in Fig. 6, as can be seen clearly from the contour plots at $t = 31.4$. In the following section, we describe a new instability mechanism derived from the Navier–Stokes equation that explains the instability induced sudden changes in load.

3.3. A new mechanism of instability

While talking about instability in general, Landahl and Mollo-Christensen (1992) noted that molecular viscosity can be destabilizing and stated that *it is possible to understand such behaviour by studying the redistribution of the total mechanical energy of the flow* [*not just how the "energy of the perturbation" given by the square of the fluctuating velocity changes locally with time*].

For incompressible flow the total pressure, p_t, is a true descriptor of the *total mechanical energy* (as described above) of the flow. It is straight-forward to rewrite the Poisson Eq. (5) for total pressure into the following

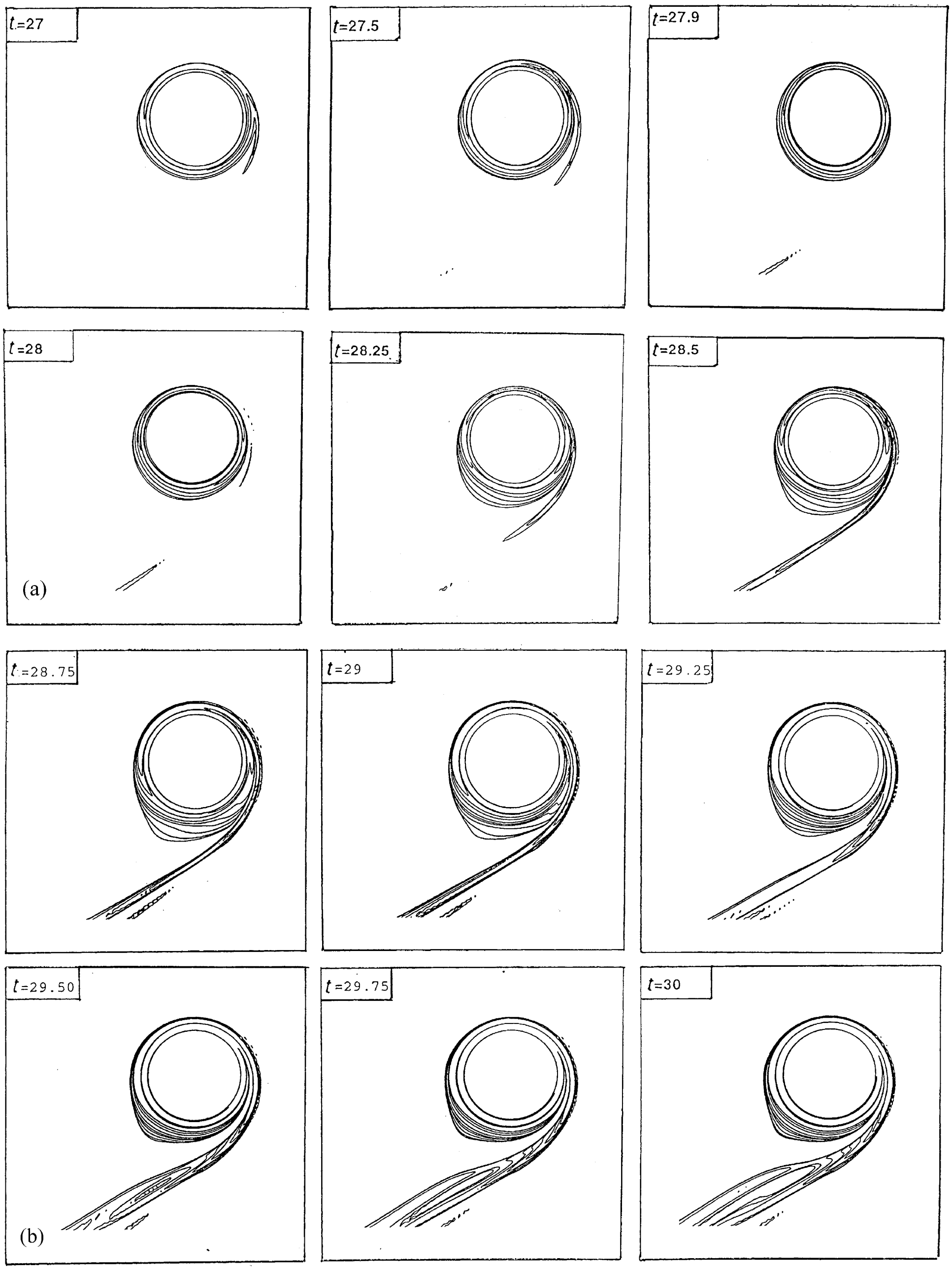

Fig. 7. Contours of the right-hand side of Eq. (12) at indicated times during the first instability. This corresponds to the case of Fig. 5.

form:

$$\nabla^2\left(\frac{p_t}{\rho}\right) = |\omega^2| + \mathbf{V}\cdot\nabla^2\mathbf{V}. \tag{10}$$

If we furthermore decompose the total pressure in terms of primary and disturbance components by

$$\frac{p_t}{\rho} = \frac{p_m}{\rho} + \frac{p_d}{\rho} \tag{11}$$

then the governing equation for the disturbance flow can be written down as

$$\nabla^2 p_d = 2\omega_m\cdot\omega_d + \mathbf{V}_m\cdot\nabla^2\mathbf{V}_d + \mathbf{V}_d\cdot\nabla^2\mathbf{V}_m. \tag{12}$$

In Eqs. (11) and (12) the subscripts m and d signify the primary and disturbance fields. Eq. (12) represents the efflux of disturbance energy across the surface of an infinitesimal control volume, constructed around the point in question. If the right-hand side of Eq. (12) is negative, then the disturbance energy at that instant of time increases and hence would correspond to an unstable situation. In Eq. (12) the right-hand side terms are thus either the source or sink of disturbance energy. Having a source is equivalent to an instability, while a sink would imply subsidence of disturbance energy. Since this is based on the instantaneous flow field, the perceived instability would be a temporal one. There are certain features of this instability, whenever it is present, that would be discussed. Firstly, this does not depend whether the primary flow is two or three dimensional. This has a very special significance then for the problem at hand. Such instability when it exists can provide a limiting mechanism for the monotonically growing circulation and it may not be due to specific three dimensionality, as conjectured by Tokumaru and Dimotakis (1993). Secondly such an instability is determined by the kinematics of the flow field only. The first term on the right-hand side of Eq. (12) is due to the interaction of the vorticity distribution of the primary and disturbance field. The second and third terms on the right-hand side of Eq. (12) arise due to interaction of the velocity field with the curl of the vorticity field. These last two terms $\mathbf{V}_m\cdot\nabla^2\mathbf{V}_d + \mathbf{V}_d\cdot\nabla^2\mathbf{V}_m$ would be referred to as T_2 for further discussion.

In the following, the instability associated with Magnus–Robins effect that was shown in Fig. 5, is explored. It is apparent that as time progresses after the impulsive start, the created vorticity increases the lift and it tends to an equilibrium state where the creation of circulation is balanced by physical dissipation. Such an equilibrium is achieved at $t = 27.67$ in Fig. 5. However, this equilibrium is unstable with respect to infinitesimal disturbances, causing the lift to fall rapidly. Subsequently, the lift increases again till it reaches a second equilibrium state. In the context of the present computations, various sources of numerical errors promote disturbance energy growth, as they are present all the time. When the equilibrium state is unstable, one sees the growth of any background disturbances present. The use of a correct numerical method that is neutrally stable with respect to numerical errors is therefore mandatory to capture the instability. The numerical solutions obtained are processed to estimate the right-hand side of Eq. (12). It is seen that the vorticity interaction term (the first term on the right-hand side) is not important. It is the term T_2 that contributes to the instability. To identify the presence of physical instabilities, in Fig. 7 the negative T_2 contours are shown. From the plotted figures it is evident that flow is unstable in the recirculating pool of fluid next to the cylinder surface at all time. However, it is not convected outside the recirculating pool till the time when T_2 becomes strongly negative. And then the velocity field convects this unstable pool of fluid out of the recirculating zone in the direction of the local velocity field. While the convection process proceeds, the recirculating region also enlarges in size, as can be seen in the streamline plots of Fig. 6 and the T_2 contours.

The relative role of $\omega_m\cdot\omega_d$ vis-à-vis T_2 can be seen from Fig. 8 where the minimum of the full right-hand side and T_2 are shown as a function of time. It is worthwhile to note that the lift minimum of Fig. 5 is exactly at the same time instant of the minimum of the curves drawn in Fig. 8.

The above instability was seen to occur for large supercritical rotation rates. That this is also possible at other Reynolds numbers is explored next. In Fig. 9, c_l and c_d variations with time are shown for the case of $\mathrm{Re} = 1000$ and $\Omega = 5$. This was the case for which some computational results were shown in Chew et al. (1995). For this case also, one can see the instability sequences. Before $t = 270$, each of the instabilities is followed by a period where lift and drag values reach constant levels. The constant drag values are almost zero, implying that the corresponding flow patterns are like the inviscid flow field. The period over which such flow patterns exist keeps diminishing at times beyond $t = 300$ and the flow is continuously unsteady.

To understand the implication of such continued unsteadiness, the Fast Fourier Transform (FFT) of the lift data of Figs. 5 and 9 are shown in Fig. 10. Both data sets represent multi-periodic response. For the $\mathrm{Re} = 1000$ and $\Omega = 5$ case, the peaks are the fundamental and its superharmonics. From the FFT of the time signal, the fundamental frequency is the first peak shown in the figure and is readily read-off as $F = 0.05612$. In Fig. 10, all the prominent peaks have been identified that are the superharmonics of this fundamental. For the $\mathrm{Re} = 3800$ and $\Omega = 5$ case, one sees additionally the

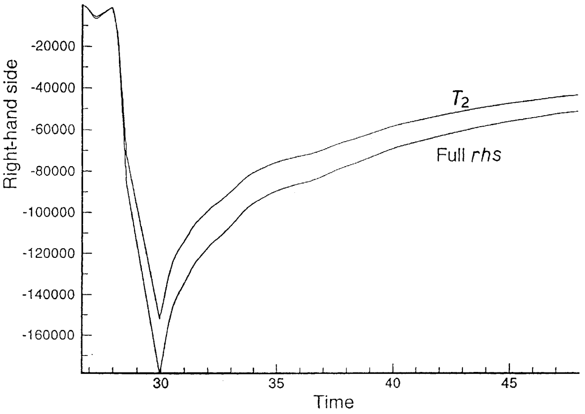

Fig. 8. Minimum value of the right-hand side of Eq. (12) plotted for the disturbance energy. Shown are the total right-hand side and the T_2 term.

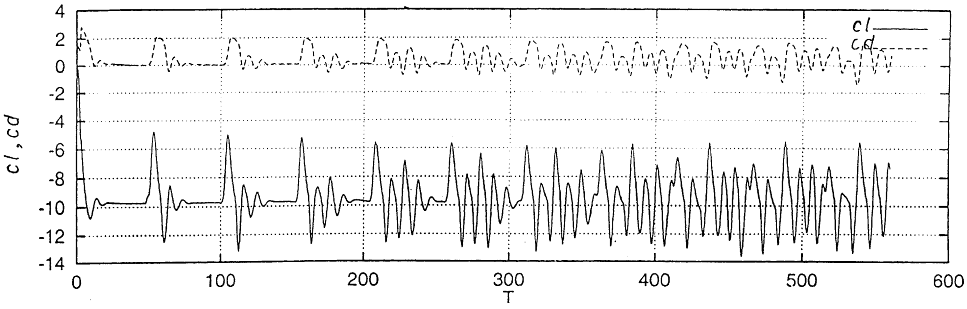

Fig. 9. Lift and drag coefficient variation with time for $\mathrm{Re} = 1000$ and $\Omega = 5$ for impulsive start case.

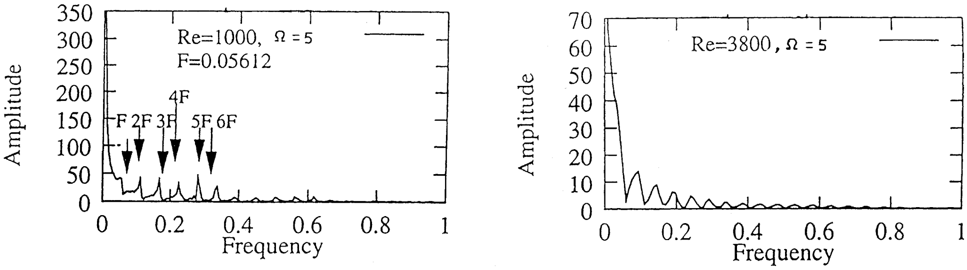

Fig. 10. FFT of c_l and c_d data shown in Figs. 5 and 9.

presence of sub-harmonics. Also in the latter case, most of the energy is confined at zero frequency, although the frequency bandwidth is much larger for the high Reynolds number case.

4. Concluding remarks

In this research, the flow past a spinning and translating cylinder is studied with the idea of exploring the lift generation and limiting mechanism via unsteady flow development. The computed results clearly display temporal instability at irregular intervals—which was reported by Werle (1984) experimentally. We have identified the cause of this temporal instability as due to an interaction between the velocity field and the curl of the vorticity field of the primary and disturbance flow fields. Such instability can be present for two-dimensional flows and hence the limiting mechanism is not necessarily by spanwise connection of the recirculating flow with the flow outside this zone. During such interactions the flow that recirculates near the cylinder shows efficient energy transport from the primary to the disturbance flow field. For a Reynolds number of 3800, the successive instabilities level off the total lift experienced by the rotating cylinder that matches excellently with measurements reported by Tokumaru and Dimotakis (1993).

The reported study of an instability mechanism for flow past a rotating cylinder reveals the limiting maximum lift generation via shedding of vortex puffs at discrete times. It would be interesting to view the general vortex-shedding phenomenon also as an instability of the same kind. This instability mechanism is more generic, as it originates from Navier–Stokes equation without any simplifying assumptions on the flow. It would not be straightforward to identify the primary and disturbance flows in a general case; however, the present study can be viewed as a prototype flow system exhibiting the features and causes of vortex shedding.

Acknowledgements

We express our sincere gratitude to Prof. Y.T. Chew of NUS who suggested this problem and was available for discussions during the course of the investigation. We would also like to thank Prof. M. Coutanceau for permitting reproduction of the experimental photograph in Fig. 2, taken from her group's published results.

References

Anderson, J.D., 1997. A History of Aerodynamics and its Impact on Flying Machines. Cambridge University Press, Cambridge, UK.

Badr, H.M., Dennis, S.C.R., 1985. Time-dependent viscous flow past an impulsively started rotating and translating circular cylinder. J. Fluid Mech. 158, 447–488.

Badr, H.M., Coutanceau, M., Dennis, S.C.R., Menard, C., 1990. Unsteady flow past a rotating circular cylinder at Reynolds numbers 1000 and 10,000. J. Fluid Mech. 220, 459–484.

Chen, Y-M., Ou, Y-R., Pearlstein, A.J., 1993. Development of the wake behind a circular cylinder impulsively started into rotatory and rectilinear motion. J. Fluid Mech. 253, 449–484.

Chew, Y.T., 1987. Flow past a rotating cylinder. In: Shuqing, Q. (Ed.), Proceedings of International Conference on Fluid Mechanics, Beijing, China. Beijing University Press, Beijing, pp. 556–560.

Chew, Y.T., Cheng, M., Luo, S.C., 1995. A numerical study of flow past a rotating circular cylinder using a hybrid vortex scheme. J. Fluid Mech. 299, 35–71.

Christiansen, J.P., 1973. Numerical simulation of hydromechanics by the method of point vortices. J. Comput. Phys. 13, 363–379.

Coutanceau, M., Menard, C., 1985. Influence of rotation on the near-wake development behind an impulsively started circular cylinder. J. Fluid Mech. 158, 399–446.

Diaz, F., Gavalda, J., Kawall, J.G., Keffer, J.F., Giralt, F., 1983. Vortex shedding from a spinning cylinder. Phys. Fluids 26, 3454–3460.

Landahl, M.T., Mollo-Christensen, E., 1992. Turbulence and Random Processes in Fluid Mechanics. Cambridge University Press, Cambridge, UK.

Magnus, G., 1853. Uber die abweichung der gesechesse. Pogendorf's Ann. der Phys. Chem. 88, 1–14.

McLaughlin, T.E., Stephen, E.J., Robinson, M.C., 1991. Pressure measurements on a rotating circular cylinder. AIAA paper AIAA-91-3265-CP, pp. 507–513.

Nair, M.T., Sengupta, T.K., 1997. Unsteady flow past elliptic cylinder. J. Fluids Struct. 11, 555–595.

Nair, M.T., Sengupta, T.K., Chauhan, U.S., 1998. Flow past rotating cylinders at high Reynolds numbers using higher order upwind scheme. Comput. Fluids 27, 47–70.

Pan, L.S., Chew, Y.T., 2002. A general formula for calculating forces on a 2-D arbitrary body in incompressible flow. J. Fluids Struct. 16, 71–82.

Perry, A.E., Chong, M.S., Lim, T.T., 1982. The vortex shedding process behind two-dimensional bluff bodies. J. Fluid Mech. 116, 77–90.

Polidori, G., Pineau, G., Meraim, K.A., Coutanceau, M., 1993. Shedding process of the initial vortices from impulsively started cylinders at Re = 1000: end and body geometry effects. In: Eckelmann, H., Graham, J.M.R., Huerre, P., Monkewitz, P.A. (Eds.), Proceedings of the IUTAM Symposium on Bluff-Body Wakes, Dynamics and Instabilities. Springer, Berlin, pp. 285–288.

Prandtl, L., 1926. Application of the "Magnus Effect" to the wind propulsion of ships. NACA TM 387.

Reid, E.G., 1924. Tests of rotating cylinders. NACA TN 209.

Roache, P.J., 1976. Computational Fluid Dynamics. Hermosa Publishers, New Mexico, USA.

Robins, B., 1761. Mathematical Tracts, Vols. 1 and 2. J. Nourse, London.

Sarpkaya, T., 1989. Computational methods with vortices—The 1988 Freeman scholar lecture. J. Fluids Eng. 111, 5–52.

Sarpkaya, T., 1994. Vortex element methods for flow simulations. In: Wu, Th., Hutchinson, A. (Eds.), Advances in Applied Mechanics, Academic Press, New York, Vol. 31, pp. 113–247.

Schneider, G.E., Zedan, M., 1981. A modified strongly implicit procedure for the numerical solution of field problems. J. Numer. Heat Transfer 4, 1–19.

Sengupta, T.K., Nair, M.T., 1999. Upwind schemes and large eddy simulation. Int. J. Numer. Methods Fluids 31, 879–889.

Sengupta, T.K., Gupta, K., Nair, M.T., 1999. Lift generation and limiting mechanism via unsteady flow development for Magnus–Robins effect. In: Cui, E. (Ed.), Proceedings of Eighth Asian Congress of Fluid Mechanics. International Academy Publishing, Beijing, pp. 413–416.

Thom, A., 1931. Experiments on the flow past a rotating cylinder. ARC R & M 1410.

Tokumaru, P.T., Dimotakis, P.E., 1993. The lift of a cylinder executing rotary motions in a uniform flow. J. Fluid Mech. 255, 1–10.

Werle, H., 1984. Hydrodynamic visualization of the flow around a streamlined cylinder with suction. Cousteau–Malavard turbine sail model. Le Recherche Aerospatiale 4, 29–38.